



Solar Orbiter and SDO Observations, and a Bifrost Magnetohydrodynamic Simulation of Small-scale Coronal Jets

Navdeep K. Panesar^{1,2} , Viggo H. Hansteen^{1,2,3,4} , Sanjiv K. Tiwari^{1,2} , Mark C. M. Cheung¹ , David Berghmans⁵ , and Daniel Müller⁶ 

¹ Lockheed Martin Solar and Astrophysics Laboratory, 3251 Hanover Street, Bldg. 252, Palo Alto, CA 94304, USA; panesar@lmsal.com

² Bay Area Environmental Research Institute, NASA Research Park, Moffett Field, CA 94035, USA

³ Rosseland Centre for Solar Physics, University of Oslo, P.O. Box 1029 Blindern, NO-0315 Oslo, Norway

⁴ Institute of Theoretical Astrophysics, University of Oslo, P.O. Box 1029 Blindern, NO-0315 Oslo, Norway

⁵ Solar-Terrestrial Centre of Excellence—SIDC, Royal Observatory of Belgium, Ringlaan -3- Av. Circulaire, B-1180 Brussels, Belgium

⁶ European Space Agency, ESTEC, P.O. Box 299, 2200 AG Noordwijk, The Netherlands

Received 2022 August 31; revised 2022 November 7; accepted 2022 November 8; published 2023 January 20

Abstract

We report high-resolution, high-cadence observations of five small-scale coronal jets in an on-disk quiet Sun region observed with Solar Orbiter’s EUV/HRI_{EUV} in 174 Å. We combine the HRI_{EUV} images with the EUV images of SDO/AIA and investigate the magnetic setting of the jets using coaligned line-of-sight magnetograms from SDO/HMI. The HRI_{EUV} jets are miniature versions of typical coronal jets as they show narrow collimated spires with a base brightening. Three out of five jets result from a detectable minifilament eruption following flux cancelation at the neutral line under the minifilament, analogous to coronal jets. To better understand the physics of jets, we also analyze five small-scale jets from a high-resolution Bifrost MHD simulation in synthetic Fe IX/Fe X emissions. The jets in the simulation reside above neutral lines and four out of five jets are triggered by magnetic flux cancelation. The temperature maps show evidence of cool gas in the same four jets. Our simulation also shows the signatures of opposite Doppler shifts (of the order of ± 10 s of km s^{-1}) in the jet spire, which is evidence of untwisting motion of the magnetic field in the jet spire. The average jet duration, spire length, base width, and speed in our observations (and in synthetic Fe IX/Fe X images) are 6.5 ± 4.0 min (9.0 ± 4.0 minutes), 6050 ± 2900 km (6500 ± 6500 km), 2200 ± 850 km, (3900 ± 2100 km), and 60 ± 8 km s^{-1} (42 ± 20 km s^{-1}), respectively. Our observation and simulation results provide a unified picture of small-scale solar coronal jets driven by magnetic reconnection accompanying flux cancelation. This picture also aligns well with the most recent reports of the formation and eruption mechanisms of larger coronal jets.

Unified Astronomy Thesaurus concepts: [Solar magnetic fields \(1503\)](#); [Solar magnetic reconnection \(1504\)](#); [Jets \(870\)](#); [Solar corona \(1483\)](#); [Solar chromosphere \(1479\)](#)

Supporting material: animations

1. Introduction

The Extreme Ultraviolet Imager (EUI; Rochus et al. 2020), on board the Solar Orbiter (Müller et al. 2020), observed numerous small-scale brightenings, known as “campfires” (Berghmans et al. 2021). Using 5 minutes of EUI data by the telescope EUV High-Resolution Imager, HRI_{EUV}, Berghmans et al. (2021) reported that the duration of campfires ranges from 10 to 200 s. They appear at coronal temperatures between 1 MK and 1.6 MK and at the bright edges of chromospheric network lanes. Using triangulation techniques, it was determined that some of the campfires are located between 1000 and 5000 km above the photosphere (Zhukov et al. 2021). However, the photospheric magnetic field environment and their evolution in relation to campfires were not known in their study.

Panesar et al. (2021) studied the dynamics and magnetic field evolution of 52 randomly selected campfires by combining EUI 174 Å images together with EUV images from SDO/AIA and line-of-sight magnetograms from SDO/HMI. They found that

(i) campfires are rooted at the edges of photospheric magnetic network lanes; (ii) most of the campfires reside above neutral lines and 77% of them appear at sites of magnetic flux cancelation between the majority-polarity magnetic flux patch and a merging minority-polarity flux patch, with a flux cancelation rate of $\sim 10^{18}$ Mx hr⁻¹; (iii) some of the smallest campfires come from the sites where magnetic flux elements were barely discernible in HMI; (iv) 79% (41 out of 52) of campfires are accompanied by structures of cool plasma, analogous to small-scale filaments in coronal jets; and (v) campfires resemble small-scale jets, loops, and dots, and some of them have a “complex” structure. They concluded that “campfire” is a general term that encompasses various types of small-scale solar features/brightenings.

Later Kahil et al. (2022) also examined the line-of-sight photospheric magnetic field evolution of campfires using Solar Orbiter’s PHI data and found similar results to Panesar et al. (2021), in that majority of campfires are triggered by magnetic flux cancelation.

Some of the campfires show similarities with coronal jets (e.g., Panesar et al. 2016b, 2018a; Hou et al. 2021; Panesar et al. 2021). They occur at the edges of quiet Sun network regions and are driven by the eruption of cool plasma structures. Further, there are several other campfire-like events that were observed by HRI_{EUV} e.g., fine-scale dots in an

emerging region (Tiwari et al. 2022), plasma jets (Chitta et al. 2021), and plasma flows (Mandal et al. 2021; Li 2022).

Similar to EUI campfires, several small-scale tiny brightenings (e.g., Alpert et al. 2016), low-lying loop nanoflares (Winebarger et al. 2013), small-scale loops/surges (Tiwari et al. 2019), and fine-scale jets (also known as jetlets; Panesar et al. 2019) have been observed by high-resolution EUV images from Hi-C (Kobayashi et al. 2014; Rachmeler et al. 2019). Jetlets occur at the edges of magnetic network lanes and they show similarities with coronal jets (Raouafi & Stenborg 2014; Panesar et al. 2018b, 2020). Although erupting minifilament-like dark structures have not been seen at the base of jetlets.

Using 3D radiation MHD simulation, Chen et al. (2021) reported that campfires are mostly caused by component reconnection between interacting bundles of magnetic field lines. In one out of seven events, they found evidence of twisted flux rope in agreement with the observational findings of Panesar et al. (2021). But in their study, Chen et al. (2021) did not provide any evidence of flux emergence or flux cancellation at the base of any of their seven analyzed campfires.

Here, we present examples of five on-disk small-scale solar coronal jets observed by the telescope HRI_{EUV} of EUI on board Solar Orbiter together with EUV images from Solar Dynamics Observatory (SDO)/Atmospheric Imaging Assembly (AIA; Lemen et al. 2012), and line-of-sight magnetograms from SDO/Helioseismic and Magnetic Imager (HMI; Scherrer et al. 2012). We find that these small-scale jets are miniature versions of larger coronal jets. The only difference is that these are four to five times smaller in size than typical coronal jets. To better understand the physics of coronal jets, we also synthesize Fe IX/Fe X emissions from a Bifrost magnetohydrodynamic (MHD) simulation. By investigating the plasma flows and magnetic field evolution in the synthetic images, we find that coronal jets reside above magnetic neutral lines, where magnetic flux convergence and cancellation normally occurs, in agreement with the observations. They often show opposite Doppler shifts (blueshifts and redshifts) at the jet spire during the eruption onset. Four out of five jets show evidence of cool plasma as we observe in the EUI and AIA images.

2. Data Sets

2.1. Solar Orbiter/EUI

We randomly selected five small-scale coronal jets in a quiet region using data from HRI_{EUV} on 2020 May 20.⁷ The observations were taken when the instrument was in the commissioning phase. The HRI_{EUV} wavelength passband is centered on 174 Å and detects the emission from Fe IX and Fe X lines that form at around 1 MK. The HRI of EUI captured high-resolution images (pixel size of 0".492; Rochus et al. 2020) at a high temporal cadence (10 s). The Solar Orbiter was positioned at 0.612 au from the Sun on 2020 May 20, thus the HRI_{EUV} images have a pixel size of 217 km. During this period of observation (between 21:20 and 22:17 UT) HRI_{EUV} captured five images at a 10 s cadence plus a 6th image 70 s later. These observations were made as a part of a technical compression test of HRI_{EUV}, therefore having variable settings. Nonetheless, 60 images are well exposed, unbinned, and

compressed at high-quality levels (Panesar et al. 2021; Tiwari et al. 2022). The HRI_{EUV} events appear 3.22 minutes earlier than the SDO/AIA images because, as mentioned, the Solar Orbiter was closer to the Sun than the SDO. The separation angle between Solar Orbiter and SDO was 16°.33.

2.2. SDO/AIA and SDO/HMI

We also use extreme ultraviolet (EUV) images captured with AIA on board SDO. AIA provides full Sun images with a high spatial resolution (1"5) and high temporal cadence (12 s) in seven EUV wavelength bands (Lemen et al. 2012). For our present study, we mainly use images from 304, 171, and 193 Å channels because the jets are best seen in these three wavelengths. To investigate the photospheric magnetic field of the jet-base regions, we use line-of-sight magnetograms from HMI (Scherrer et al. 2012). In addition to other data products, HMI provides full-disk line-of-sight (LOS) magnetograms at a 45 s temporal cadence with pixels of 0".5. The HMI magnetograms have a noise level of about ± 7 G (Couvidat et al. 2012; Schou et al. 2012). We summed two consecutive magnetograms to enhance the visibility of weak magnetic flux patches.

The AIA and HMI data sets have been downloaded from the JSOC⁸ cutout service and coaligned using SolarSoft routines (Freeland & Handy 1998). JHelioviewer software was also used to locate the jets in SDO/AIA (Müller et al. 2017).

2.3. Bifrost Simulation

We analyze a Bifrost magnetohydrodynamic (MHD) simulation of a quiet Sun network region to better interpret the structure and dynamics of coronal jets and the observations. For more details on this particular simulation, see papers by De Pontieu et al. (2022) and Tiwari et al. (2022). A horizontal flux sheet of varying strength is injected at the bottom boundary of a model that spans a domain of $72 \times 72 \times 61$ Mm³ on a grid of [720, 720, 1115] using the Bifrost code (Gudiksen et al. 2011). The model reaches 8.5 Mm below the photosphere and then extends up to 52.5 Mm into the corona, above the photosphere. The scattering in the chromosphere with an optically thick radiative transfer is included in the Bifrost model (e.g., Skartlien 2000; Hayek et al. 2010). The model includes optically thin radiative transfer in the middle chromosphere to the corona following the methods described by Carlsson & Leenaarts (2012). The equation of state (together with partial ionization of the atmospheric plasma) is treated in local thermodynamic equilibrium (LTE) through a look-up table that is constructed using solar abundances.

Importantly, thermal conduction along the magnetic field, particularly relevant for the solar corona, is included in the energy equation. We synthesize Fe IX and Fe X emissions by integrating the contribution function $\phi(u, T)n_e n_H G(T, n_e)$ along the line of sight. Here, $\phi(u, T) = 1/\sqrt{(\pi)} \Delta\nu_D \exp[-((\Delta\nu - \nu u \cdot n/c)/\Delta\nu_D)^2]$, where $\Delta\nu = \nu - \nu_0$, with ν_0 being the laboratory frequency of the transition involved, $u \cdot n$ is the velocity along the line of sight. The thermal broadening profile corresponds to a width $\Delta\nu_D = \nu_0/c\sqrt{(2kT/m_A)}$, where m_A is the mass of the radiating atom, and T is the temperature. The values are obtained along the line of sight from the simulation and then the contribution function is integrated along the line of sight for every frequency

⁷ <https://doi.org/10.24414/z2hf-b008>

⁸ <http://jsoc.stanford.edu/ajax/exportdata.html>

Table 1
Properties of Observed and Simulated Coronal Jets

Event No.	Time (UT)	Jet Duration (min)	Jet Spire Length (km)	Jet-base Width (km)	Visibility of Cool Plasma	Flux Cancellation	Speeds (km s^{-1})
Jets in the EUV Observations ^d							
1	21:20:52	2 ± 10 s	3800 ± 325	1900 ± 200	No	A ^a	47 ± 5.0
2	21:48:12	7 ± 10 s	7650 ± 260	3700 ± 2450	A ^b	A ^a	55 ± 9.0
3	22:13:02 ^c	13 ± 10 s	10400 ± 810	1900 ± 780	Yes	Yes	65 ± 10.0
4	22:05:02 ^c	8 ± 10 s	5000 ± 160	2000 ± 225	Yes	Yes	58 ± 0.5
5	21:38:22 ^c	3 ± 10 s	3300 ± 350	1500 ± 240	Yes	Yes	69 ± 5.0
average $\pm 1\sigma_{ave}$		6.5 ± 4.0	6050 ± 2900	2200 ± 850			59 ± 8.5
Jets in the Simulation							
1	t0+5000 s	13 ± 50 s	11200 ± 390	5780 ± 110	Yes	Yes	43 ± 1.4
2	t0+4900 s	6.6 ± 50 s	5390 ± 445	3100 ± 160	Yes	No flux	40 ± 5.0
3	t0+6850	9 ± 50 s	4130 ± 120	1770 ± 80	No	Yes	12 ± 2.5
4	t0+3600	14 ± 100 s	7500 ± 1900	6600 ± 400	Yes	Yes	72 ± 9.0
5	t0+4500	4 ± 50 s	4400 ± 190	2160 ± 150	Yes	Yes	40 ± 7.0
average $\pm 1\sigma_{ave}$		9.0 ± 4.0	6500 ± 2900	3900 ± 2100			41.5 ± 21.0

Notes.

^a Ambiguous, cancelation between weak flux elements.

^b Ambiguous, cool structure appears but does not erupt.

^c These jets are taken from Panesar et al. (2021).

^d Except the plane-of-sky speeds, which are estimated using AIA 171 Å images.

point (Hansteen et al. 2010). The ionization and excitation states of the emitting ions are taken from CHIANTI (Dere et al. 1997; Young et al. 2003). For more details see papers by Hansteen et al. (2010, 2015). Since the wavelength of the iron lines is short, there is the possibility of absorption from neutral gas. We include this effect in our calculation by multiplying the contribution function along the line of sight with $\exp(-\tau)$ where τ is the combined opacity of hydrogen and helium, as well as from singly ionized helium (see De Pontieu et al. 2009 for details).

We analyzed five small-scale jets from the simulation. We mainly use synthetic Fe IX and Fe X lines for our jet study because Fe IX and Fe X lines are the main lines of the HRI_{EUV} 174 Å passband. We note that the EUV 174 Å passband also includes emission from oxygen lines formed at roughly 280,000–320,000 K. Such emission will affect our synthetic spectra, but trial calculations indicate that they will not significantly change our analysis. Further, we also averaged synthetic Fe IX and Fe X lines and create a single map Fe IX/Fe X, in order to maintain the similarity with the HRI_{EUV} observations. Similarly, we also average two Doppler maps (for Fe IX and Fe X) to create a single Doppler map. To study the magnetic field evolution of jets in the simulation we use Bz maps (vertical component of the magnetic field) as the same field of view as Fe IX/Fe X maps and Doppler maps. This is a large-scale simulation with a pixel size of 100 km and a temporal cadence of 50 s.

3. Results

3.1. Overview

We examine the dynamics and evolution of five on-disk small-scale coronal jets observed by Solar Orbiter/EUV and SDO/AIA. Their jet-base photospheric magnetic field structure is examined by using line-of-sight magnetograms from SDO/HMI. Further, to better understand the dynamics and magnetic

field evolution of small-scale jets and to better interpret the observations, we studied five coronal jets from a high-resolution Bifrost magnetohydrodynamic (MHD) simulation. In Section 3.2 we show two examples of EUV jets from the observations, and in Section 3.3, we present two example jets from the Bifrost MHD simulation. Table 1 shows the measured parameters of all our jets observed by Solar Orbiter/EUV and found in the simulation.

3.2. Solar Orbiter and SDO Observations of Coronal Jets

3.2.1. Example 1

In Figure 1, we display a jet example 1 (event 2 of Table 1) observed by EUV and AIA. The corresponding animation shows the same images over the duration of the event. The jet is clearly visible in AIA 171 and 193 Å images but it does not show up as clearly as in AIA 304 Å image (Figure 1(a)).

The EUV jet starts with a base brightening that appears at the neutral line at 21:44:12 (green arrow in Figure 1(b)) and then a bright spire develops slowly (cyan arrow). The total duration of the jet is 7 minutes. Jet base brightening and jet spire can also be seen in the AIA 171 and 193 Å images. AIA images also show a cool plasma structure at the jet-base region (white arrow in Figures 1(e), (i)), which could be a signature of the minifilament structure as it is rooted above the magnetic neutral line. To see the evolution of the minifilament, we created a time–distance map shown in Figure 3(a). We noticed that it does not erupt and it appears right next to the jet bright point (JBP). However it is not clear whether the cool plasma structure is a minifilament because (i) it is not an erupting structure as happens in typical coronal jets and (ii) the JBP usually appears underneath the erupting minifilament (Sterling et al. 2015; Panesar et al. 2016b).

Coaligned HMI magnetograms show that the small-scale jet occurs at the edge of the positive-polarity flux patch

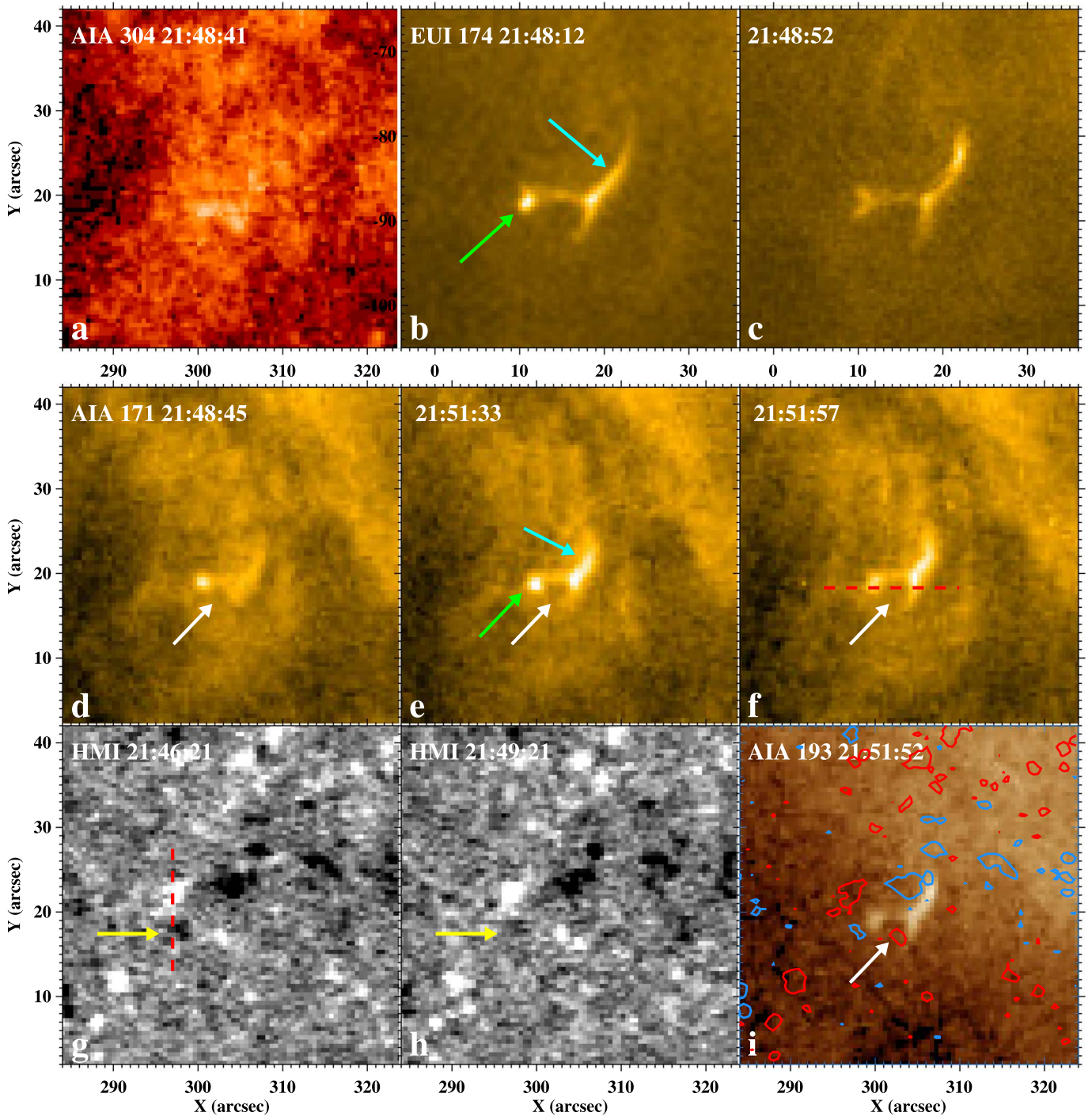


Figure 1. Example 1 of the small-scale coronal jet (event 2 of Table 1). Panels (b) and (c) show the 174 \AA HRI_{EUV} images of the jet. Panels (a), (d–f), and (i) show the same jet in AIA 304, 171, and 193 \AA images, respectively. The cyan and green arrows, respectively, point to the jet spire and jet base brightening. The white arrow points to the minifilament structure. Panels (g) and (h) display the line-of-sight photospheric magnetic field of the jet-base region. The yellow arrows point to the jet-base minority-polarity negative magnetic flux patch that converges toward the neutral line. In panel (i), HMI contours, of levels $\pm 15 \text{ G}$, at 21:46:21 UT are overlaid, where red and blue contours outline positive and negative magnetic flux, respectively. The red dashed lines in (f) and (g), respectively, show the cut for the time–distance map of Figures 3(a) and 3(b). An animation of this Figure is available. The real-time duration of the animation is 6 s but the first 2 s show the evolution of the 174 \AA HRI_{EUV} images, panels (b) and (c). The sequence runs from 21:40 to 21:54 UT. The last 4 s of the animation are of the AIA images, panels (a), (d–f), and (i). This portion of the animation runs from 21:40 to 22:00 UT. The animation is unannotated and the FOVs are the same as in this Figure.

(An animation of this figure is available.)

where the negative-polarity flux patch is also present next to it (see yellow arrows in Figure 1(g)). The negative-polarity flux patch seems to converge toward the neutral line and cancels with the positive flux patch. Figure 3(b) shows the time–distance map of the jet-base region—it shows a clear

convergence of the negative-polarity flux patch toward the positive flux patch, which triggers the jet eruption. Although we are looking at the detection limit of the HMI magnetograms, it could be a possible signature of flux convergence and cancellation.

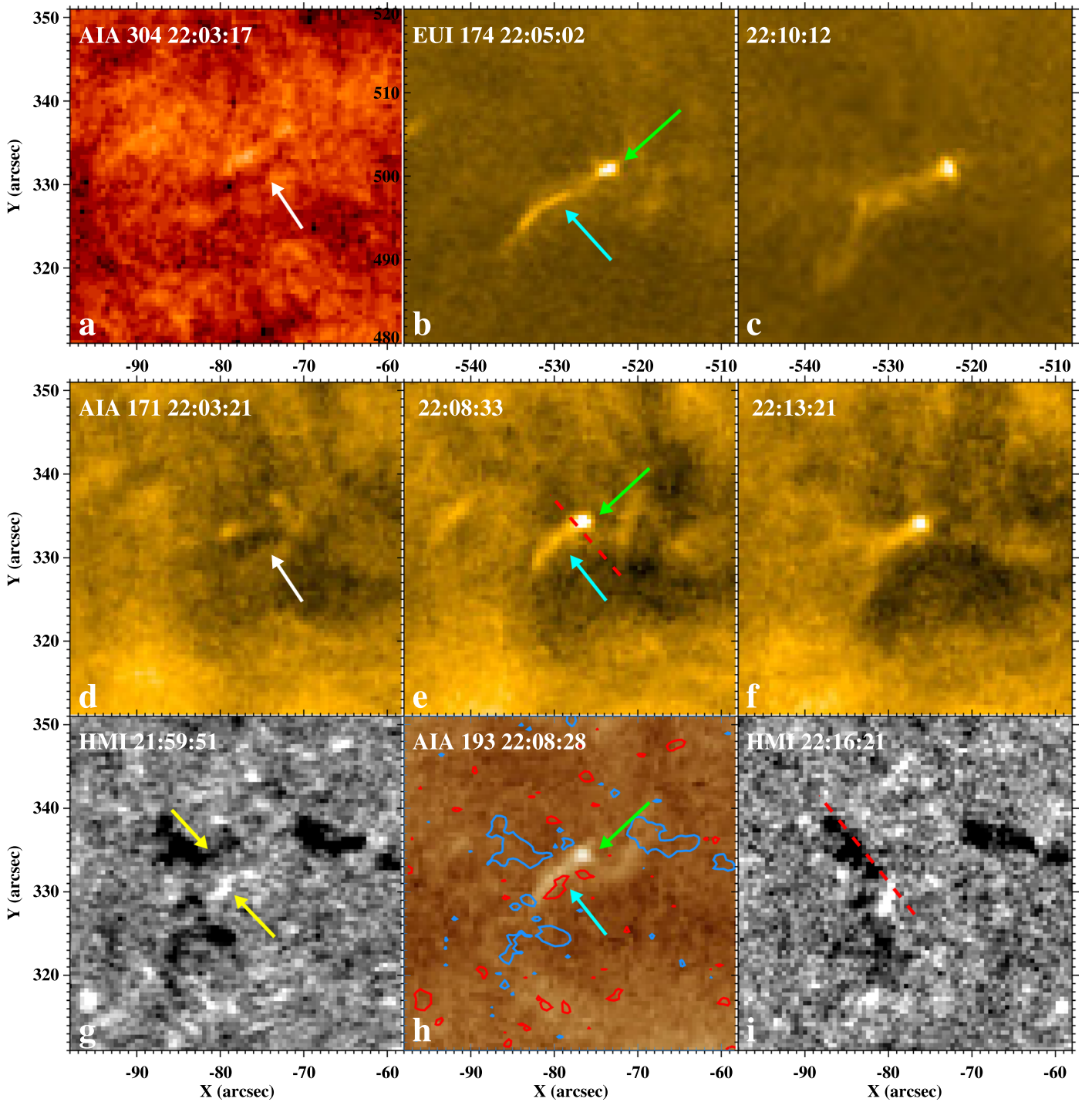


Figure 2. Example 2 of the small-scale coronal jet (event 4 of Table 1). Panels (b) and (c) show the 174 \AA HRI_{EUV} images of the jet. Panels (a), (d–f), and (h) show the same jet in AIA 304, 171, and 193 \AA images, respectively. The cyan and green arrows, respectively, point to the jet spire and jet base brightening. The white arrow points to the minifilament structure. Panels (g) and (i) display the line-of-sight photospheric magnetic field of the jet-base region. The yellow arrows point to converging positive and negative flux patches where the minifilament resides. In panel (h), HMI contours, of levels $\pm 15 \text{ G}$, at 21:59:51 UT are overlaid, where red and blue contours outline positive and negative magnetic flux, respectively. The red dashed lines in (e) and (i), respectively, show the cut for the time–distance map of Figures 3(c) and 3(d). An animation of this Figure is available. The real-time duration of the animation is 10 s but the first 4 s show the evolution of the 174 \AA HRI_{EUV} images, panels (b) and (c). The sequence runs from 21:46 to 22:17 UT. The last 6 s of the animation are of the AIA images, panels (a), (d–f), and (i). This portion of the animation runs from 21:53 to 22:21 UT. The animation is unannotated and the FOVs are the same as in this Figure.

(An animation of this figure is available.)

3.2.2. Example 2

In Figure 2, we show another example of a small-scale coronal jet from our list (event 4 of Table 1). The EUI images and the corresponding animation show the jet that starts with a

base brightening (green arrow) and is followed by a jet spire (cyan arrow). This jet is also discernible in the AIA images (Figure 2 and the animation). Interestingly, AIA images also show a nice minifilament structure (at 22:01:21 in the later

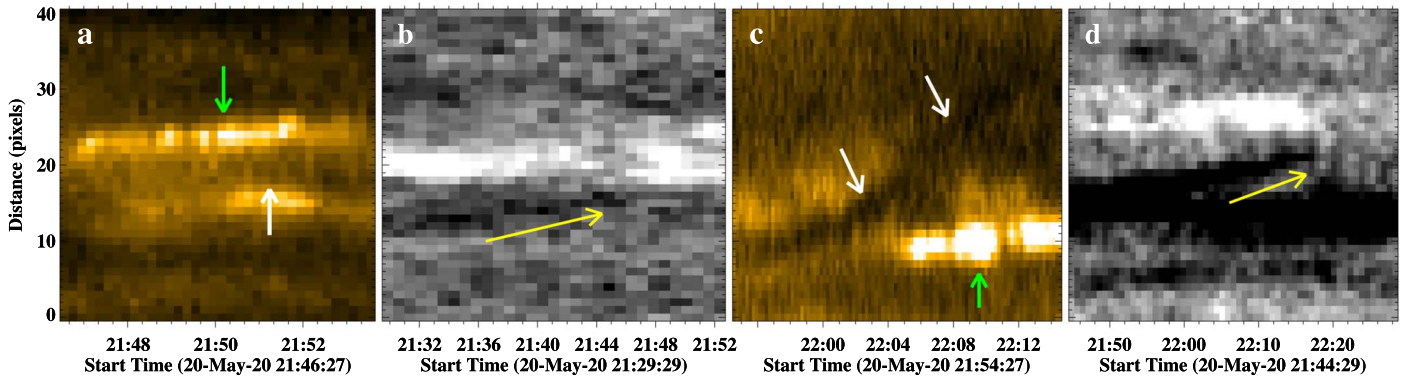


Figure 3. Panels (a) and (b), respectively, show the AIA 171 Å intensity and HMI time–distance maps of the minifilament and magnetic field of the jet in Figure 1. AIA 171 Å and HMI time–distance maps are plotted along the red dashed lines of Figures 1(f) and 1(g), respectively. Panels (c) and (d) show the AIA 171 Å intensity and HMI time–distance maps, respectively, of the jet in Figure 2. AIA 171 Å intensity map (c) is plotted along the red dashed line of Figure 2(e), where HMI map (d) is plotted along the red dashed line of Figure 2(i). The green and white arrows, respectively, point to the jet base brightening and minifilament. The yellow arrows in (b) and (d) point to the track of negative flux that converges toward the neutral line.

portion of the animation, white arrow in Figures 2(a), (d)) at the base of the jet before and during the jet eruption. The minifilament starts to rise at 22:01:57 and then a base brightening appears where the minifilament was rooted prior to its eruption. The evolution of the minifilament and JBP can be seen in the time–distance map of Figure 3(c). It shows the clear rise of the minifilament structure and the appearance of the base brightening underneath it. This scenario is similar to typical coronal jets, in which a coronal jet is driven by the eruption of a minifilament. This is an example of a small-scale coronal jet (base width 2000 ± 225 km) that is driven by a minifilament eruption. The observed spire length (5000 ± 160 km) of this jet is shorter than our IRIS jetlet spire lengths (Panesar et al. 2018b) and similar to the spire length of some of the Hi-C jetlets (Panesar et al. 2019). Whereas the observed jet-base width is shorter than the jet-base width of typical coronal jets (Panesar et al. 2016b, 2018a). The jet propagates outward with an average speed of 58 ± 0.5 km s⁻¹.

The pre-jet minifilament lies above the magnetic neutral line between the negative flux patch and positive magnetic flux patch (yellow arrows in Figure 2(g)). Both negative and positive flux patches are seen to converge toward the neutral line (Figure 2(i)). The HMI time–distance map presents the scenario of flux convergence and cancellation at the jet-base region (Figure 3(d)). Possible flux convergence and cancellation trigger the pre-jet minifilament eruption.

3.2.3. Physical Properties

We estimated the physical properties, e.g., jet duration, spire length, and spire width, of our small-scale jets using EUV 174 Å images (Table 1). The duration of each jet was calculated when the jet base brightening was turned on until the spire faded away. The spire length is measured from the base to the visible tip of the spire at the time of its maximum extent. The jet-base width is estimated at the widest part of the base during its peak brightening. The average duration of our five jets is 6.5 ± 4 minutes, which is typical for small-scale jets as also reported by Hou et al. (2021) using Solar Orbiter/EUV data. The average jet spire length comes to be 6050 ± 2900 km, which is smaller than the Hi-C 2.1 jet-like events (Panesar et al. 2019). Whereas the average jet-base width is 2200 ± 850 km, which is similar to the base width of EUV campfires (Panesar et al. 2021). The average plane-of-sky speed of our jets is 60 ± 8 km s⁻¹, which

is similar to the jet speeds reported by Panesar et al. (2018b, 2019) and Hou et al. (2021). The observational speeds are estimated using AIA 171 Å images because, as previously mentioned, some of the EUV 174 Å frames are binned and have variable compression settings. Also because the EUV 174 Å images are not isochronal (Tiwari et al. 2022).

3.3. Coronal Jets in Bifrost MHD Simulation

Using a Bifrost simulation, we synthesized Fe IX and Fe X emissions to calculate line intensities and Doppler speeds. We also analyze the vertical component of the magnetic field, B_z . This is the same set of simulation that has been analyzed by Tiwari et al. (2022) for exploring the thermal, velocity, and magnetic properties of fine-scale bright dots. The simulation data is available for several hours but we analyzed the data for only 2 hr (starting simulation frame no. 420–576) at a 50 s cadence. The selected jets in our simulation have similar sizes as the observed small-scale jets, selected intentionally for a fair comparison.

3.3.1. Example 1

In Figure 5 and its corresponding animation, we display our first example of a coronal jet from simulation (event 4 of Table 1). The upper panels (a–e) show the jet in synthesized Fe IX/Fe X emission. The jet shows a bright base (green arrow in Figure 5(c)) and spire (cyan arrow in Figure 5(b)) similar to the EUV jets. The duration of this jet is 14 minutes ± 100 s, the jet-base width is 6600 ± 400 km, and the spire length is 7500 ± 1900 km. These estimations are done in the same way as done for observations.

The jet resides above the magnetic neutral line between the positive- and negative-polarity flux patches (Figure 5(a)). The bright jet base occurs at the neutral line similar to that of observations. We follow the evolution of the B_z maps with time and notice that positive and negative flux converge toward the neutral line. The flux cancellation between these two flux patches likely drives the jet. Further, to follow the evolution of the jet-base magnetic field region more clearly, we created a B_z time–distance map (Figure 6(a)) along the yellow arrow of Figure 5(g). The B_z time–distance map shows that positive and negative flux patches start to converge toward the neutral line before the jet onset. It continuously converges and cancels even after the jet eruption. The simulation shows a clear example of flux cancellation at the jet-base region and that flux cancellation

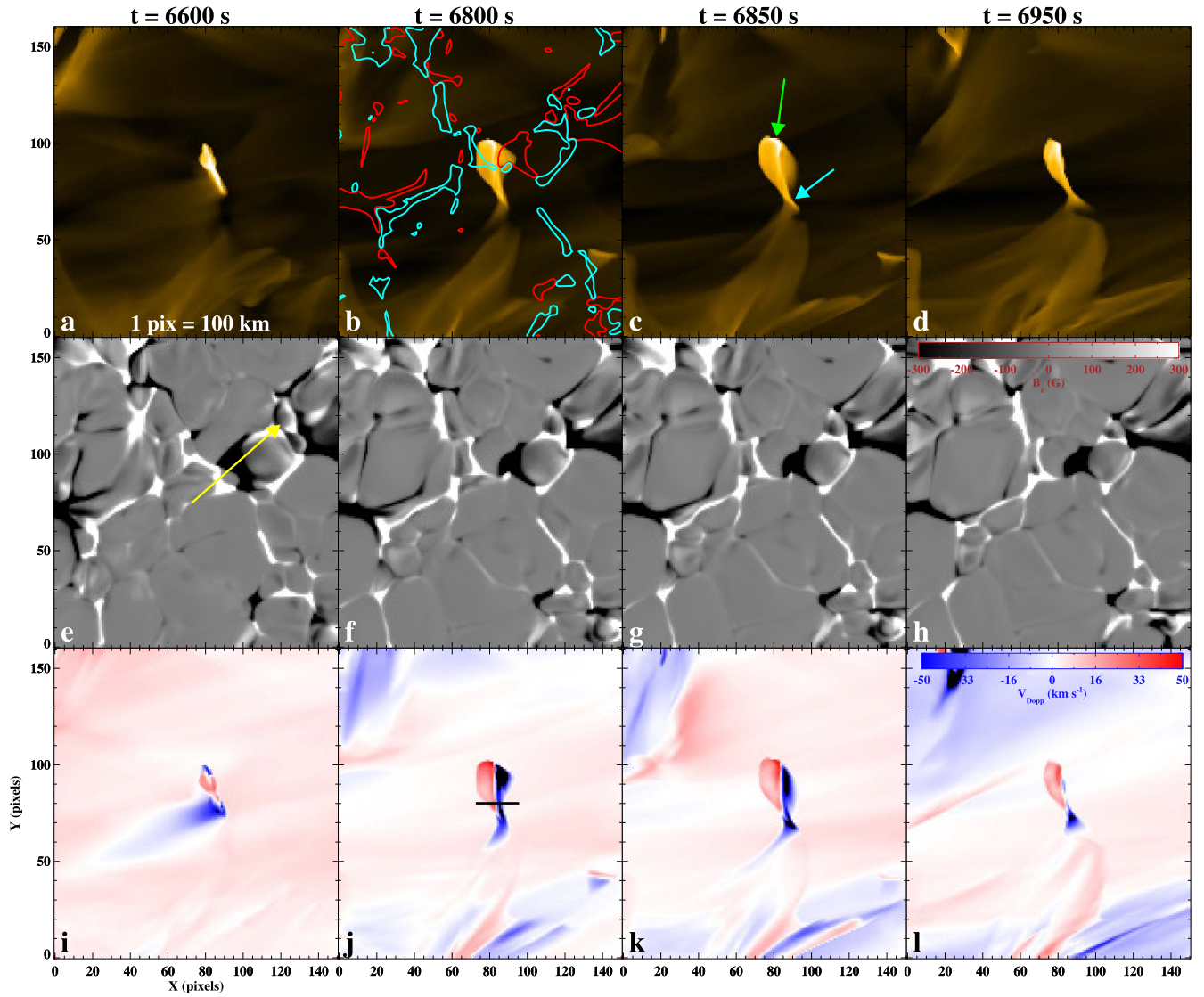


Figure 4. Coronal jet example 2 from the Bifrost MHD simulation (event 3 of Table 1). Panels (a–d) show the jet in synthesized Fe IX/Fe X emission. Panels (e–h) show the B_z map of the jet-base region. Panels (i–l) display the Fe IX/Fe X Dopplershift, v_{Dopp} , with the upper and lower values saturated at 50 km s^{-1} . The contours, of levels $\pm 200 \text{ G}$, of B_z are overlaid on panel (b), where turquoise and red contours outline positive and negative magnetic flux, respectively. The cyan and green arrows in (c) point to the jet spire and jet base brightening, respectively. The yellow arrow in (e) shows the diagonal cut along which the time–distance map is plotted and shown in Figure 6(b). The black line in (j) shows the east–west cut for the time–distance map of Figure 7(b). An animation of this Figure is available. The animation runs from 6400 s to 7050 s and is unannotated. The real-time duration is 1 s.

(An animation of this figure is available.)

leads to the jet. This behavior is in agreement with the observations of many coronal jets that are also seen to trigger flux cancellation (e.g., Shen et al. 2012; Adams et al. 2014; Panesar et al. 2016b; Sterling et al. 2017; Panesar et al. 2018a; McGlasson et al. 2019). Furthermore, we noticed another jet (jet 5 of Table 1) eruption from the same neutral line, which occurs due to continuous flux cancellation. It is common to see sequential coronal jet eruptions from the same neutral line due to continuous flux cancellation (Panesar et al. 2017, 2018b)—the jetting stops when one of the polarities fully disappears/cancels from the neutral line. Thus, in the end, there is no neutral line and there are no more jets.

Figures 5(k–o) display the Fe IX/Fe X Doppler velocity maps of the jet. The Dopplergrams show downflows (redshifts) at the base of the jet. Whereas the two opposite Doppler shifts (blueshifts and redshifts) were seen on the two edges of the jet

spire (Figure 5(m)). The opposite Doppler shifts in the jet spire are often a signature of the untwisting motion of the magnetic field in the jet spire (e.g., Pike & Mason 1998; Kamio et al. 2010; Curdt et al. 2012; Cheung et al. 2015; Tiwari et al. 2018; Sterling et al. 2019; Panesar et al. 2022). The redshifts at the base of the jet are considered to be a signature of downflows at the location of the JBP (in the reconnected closed loops; Tiwari et al. 2019; Panesar et al. 2022).

To present a quantitative picture of Doppler flows along the jet spire, we make the Doppler speed plots. For that purpose, we take a cut across the jet spire (black line in Figure 5(m)) and plot their Doppler speeds in Figure 7(a). The jet spire shows stronger blueshifts reaching up to 35 km s^{-1} and redshifts peaking at 10 km s^{-1} . Similar but stronger (up to 75 km s^{-1}) Doppler flows have been reported by Tiwari et al. (2022) in bright dots of Fe IX/Fe X emission.

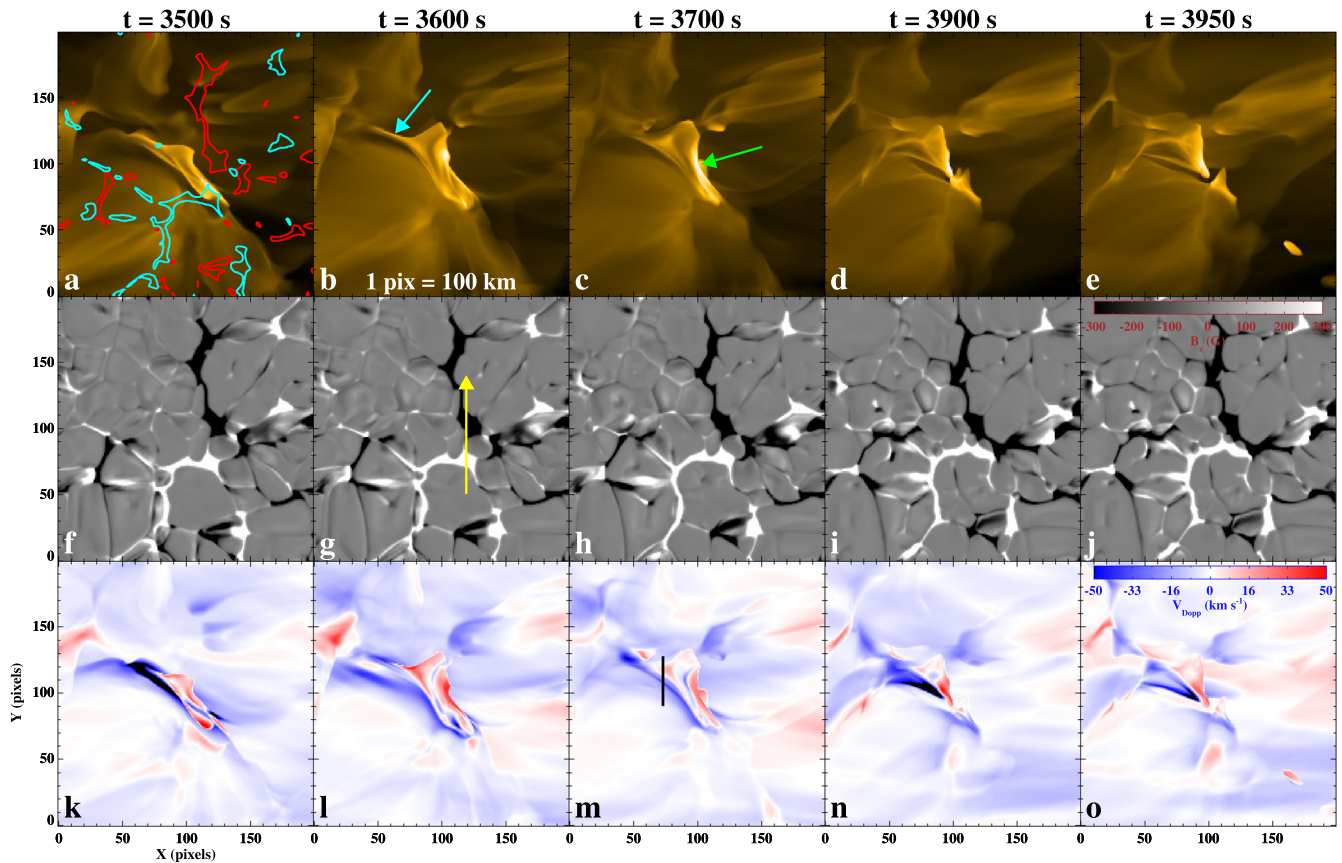


Figure 5. Coronal jet example 1 from the Bifrost MHD simulation (event 4 of Table 1). Panels (a–e) show the jet in synthesized Fe IX/Fe X emission. Panels (f–j) show the B_z map of the jet-base region. Panels (k–o) display the Fe IX/Fe X Dopplershift, v_{Dopp} , with the upper and lower values saturated at 50 km s^{-1} . The contours of levels $\pm 200 \text{ G}$ of B_z are overlaid on panel (a), where turquoise and red contours outline positive and negative magnetic flux, respectively. The cyan and green arrows in (b) and (c) point to the jet spire and jet base brightening, respectively. The yellow arrow in (g) shows the north–south cut along which the time–distance map is plotted and shown in Figure 6(a). The black line in (m) shows the north–south cut for the time–distance map of Figure 7(a). The animation runs from 3250 to 4300 s and is unannotated. The real-time duration is 1 s.

(An animation of this figure is available.)

3.3.2. Example 2

In Figure 4, we present a second example of a coronal jet from our simulation (event 3 of Table 1). The corresponding animation shows the same jet over the duration of the event. This is the smallest jet from our simulation. The jet starts with a base brightening (green arrow) and a spire (cyan arrow) that expands with time. Jet becomes maximum in size at about 6850 s (Figure 4(c)). After that, it begins to fade away. The lifetime of the jet is $9 \text{ minutes} \pm 50 \text{ s}$. It has a base width of $1770 \pm 80 \text{ km}$, and a spire length of $4130 \pm 120 \text{ km}$.

In agreement with the above example, this jet occurs at the neutral line and the JBP straddles above the neutral line (Figure 4(b)). The B_z maps show a clear scenario of flux convergence and cancellation at the jet-base region (Figures 4(e)–(h)), which leads to the jet. In Figure 6(b), we show a Bz time–distance map that is created along the diagonal arrow of Figure 4(e) to display the magnetic field evolution of the jet-base region. One can see that both the flux patches clearly converge and cancel and that flux cancellation triggers the jet. The positive flux patch has completely been eaten up by the negative flux patch. Hence no more jets occur from this location.

The Fe IX/Fe X Doppler velocity maps of this jet example are shown in Figures 4(i)–(l). In the beginning phase of the jet, dominant redshifts are observed. Later, both redshifts and

blueshifts are seen in the jet structure (Figures 4(j), (k)). The blueshift and redshift next to each other are consistent with the untwisting motions as seen in typical jet observations. For example, in Figures 4(j), (k), the extended blueshift in the southeast direction corresponds to the jet spire and the redshift and blueshift at the base extending to the jet spire corresponds to untwisting motion. Doppler speed plot is shown in Figure 7(b), which is made along the horizontal line of Figure 4(j). It shows the quantitative behavior of the Doppler flows in the jet spire. The plot shows the stronger blueshifts in the jet spire that reaches up to 50 km s^{-1} , whereas redshift goes up to 30 km s^{-1} . Similar but weaker Doppler flows have been reported by Panesar et al. (2022) in a quiet region coronal jet captured by IRIS in Mg II k spectra.

3.3.3. Temperature Maps

As mentioned in Section 2, in our simulation there is a possibility of absorption from neutral gas due to the shorter wavelength of iron lines. Therefore, we also compute the intensities of Fe IX and Fe X lines with absorption turned on. This will give us an idea if there is any chromospheric cool gas/plasma present at heights of $>2 \text{ Mm}$.

Figures 8(a)–(c) display the temperature maps of the jet of Figure 5, at different times. The jet spire and jet base are shown by cyan and green arrows, respectively. These maps also show

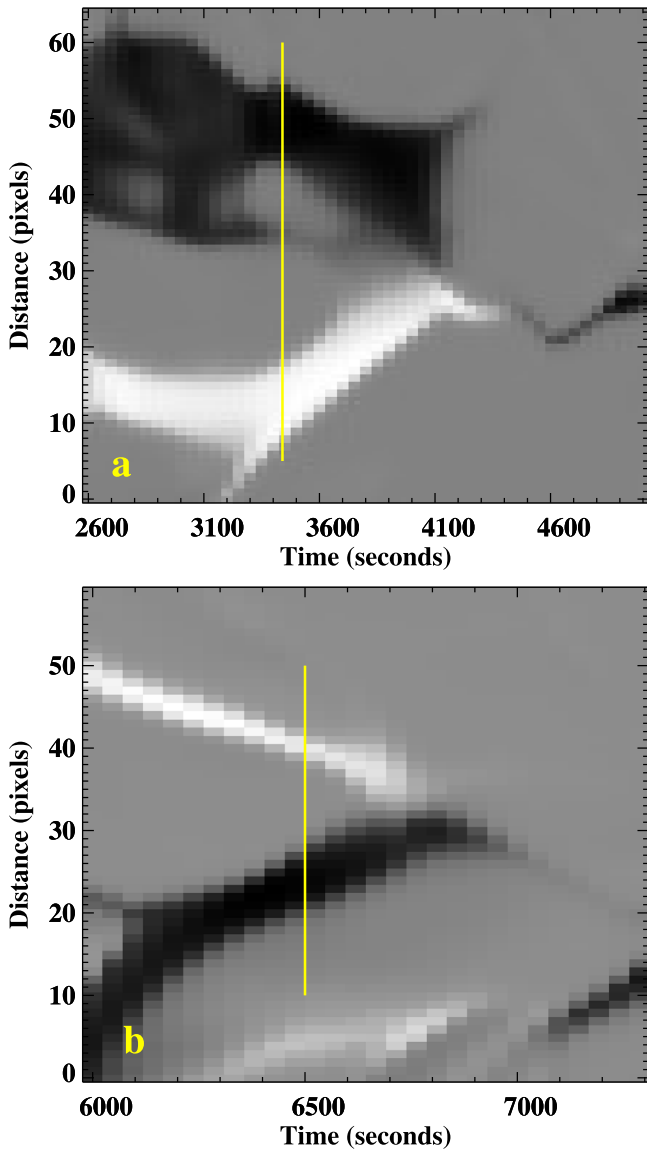


Figure 6. Magnetic field evolution. Panels (a) and (b) show the B_z time–distance maps along the yellow arrows in Figures 5(g) and 4(e), respectively. The solid yellow lines mark the onset of the jet that is shown in Figures 5 and 4. The maps show the flux convergence and cancellation at the jet-base region.

the presence of chromospheric cool plasma during the eruption onset. The cool plasma (white arrows) can be seen on the top of the jet spire when the jet is moving outwards. This scenario is in agreement with our EUV and AIA jet observation, where we also observe erupting cool plasma (minifilament) during the jet onset (Figure 2). This cool plasma structure has some similarities with the cool plasma previously seen by Hansteen et al. (2019) in simulations of UV bursts. However, the reconnection that happens in our model, on large scales, is between the newly emerged field and ambient coronal field, so there is not as much “cool” material in between the observer and the reconnection site as there was in Hansteen et al. (2019). There was 5 to 10 Mm of cold ($T < 10^4$ K) high opacity material between the reconnection location (at low to moderate heights, 0–2 Mm above the photosphere) between two different bubbles of the emerging field and the corona in Hansteen et al. (2019).

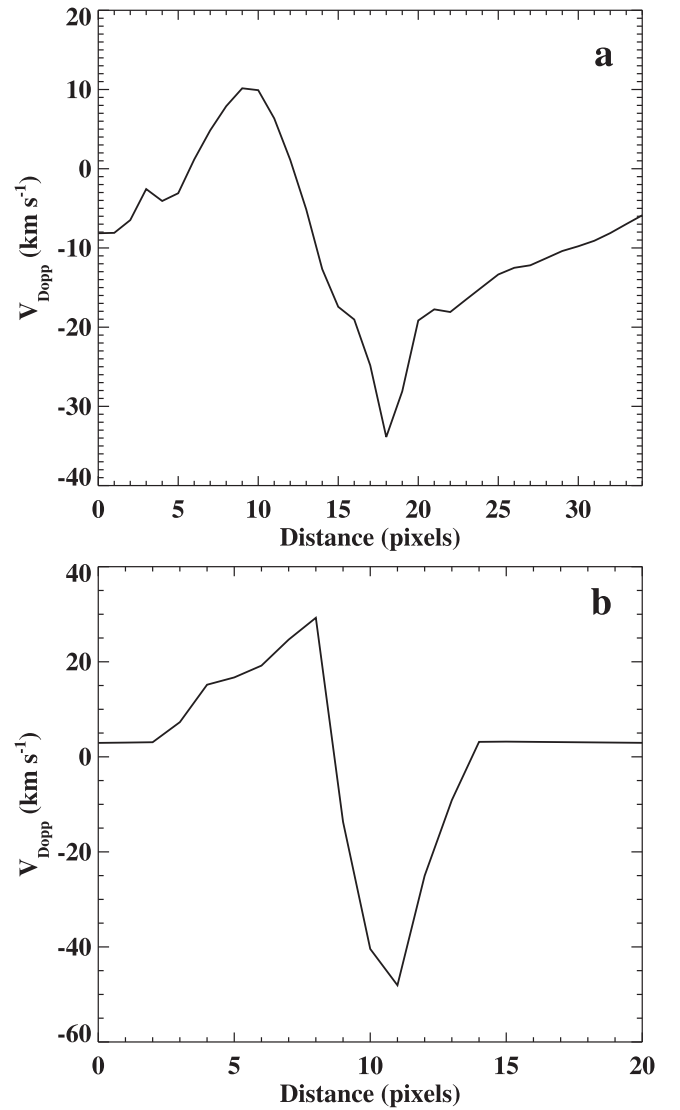


Figure 7. Doppler velocities of the jet spire. Panels (a) and (b) show the Doppler profiles of the jet spire along the black lines in Figures 5(m) and 4(j), respectively. The profiles clearly display the upflows (blueshifts) and downflows (redshifts) in the jet spire. In these plots, 1 pixel corresponds to 100 km.

In Figures 8(d)–(f), we show the temperature maps for the jet of Figure 4. This is the smallest jet example of our simulation and we can see that it does not go high on the z -axis. The jet spire and jet base are pointed with an arrow. Unlike the previously described jet, this jet does not show the presence of cool plasma. One possibility is that the jet size is so small, therefore it is hard to detect the cool plasma in it. Another reason is that maybe there is no cool plasma present in this jet.

We investigated five jets in simulation and found that most of them are similar to the observations. Similar in the sense that four out of five jets occur at the neutral line where flux cancellation takes place and four out of five jets confirm the presence of erupting cool plasma. Their durations, spire lengths, base widths, and speeds are also more or less in the range of observed EUV jets (see Table 1).

3.3.4. Magnetic Field Topology

We used the visualization software VAPOR (Li et al. 2019), to trace the magnetic field lines of our jets. 3D magnetic field

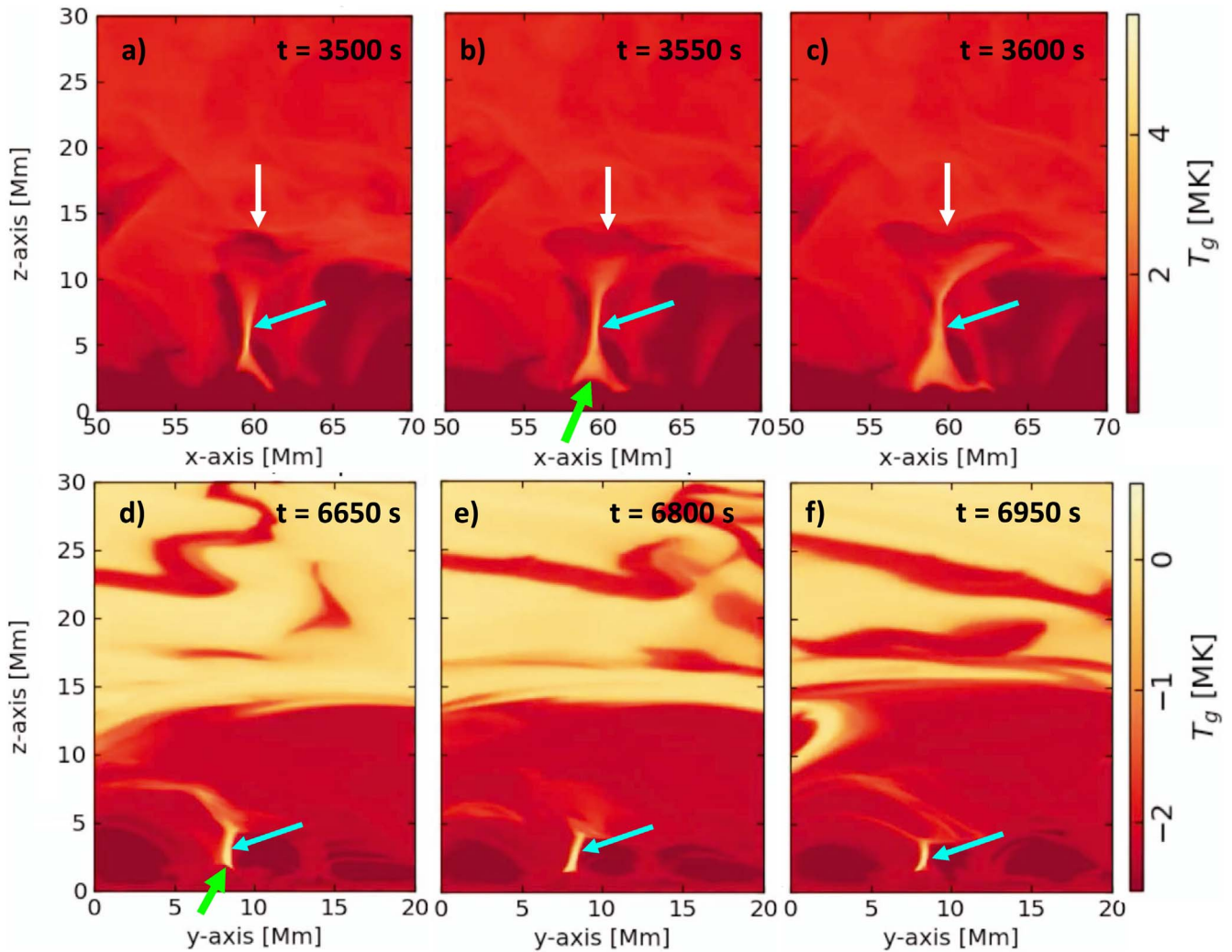


Figure 8. Temperature maps. Panels (a–c) and (d–f), respectively, show the temperature maps for the coronal jet of Figures 5 and 4. These maps are created across the jet structure vs. height (in z -direction). The z -axis corresponds to the height above the photosphere ($z = 0$). The temperature is logarithmic in units of MK, where 1 MK is zero, 0.1 MK is 100,000 K or -1 , and so on. The “g” stands for gas in T_g . The color bar scale in the top row, panels (a–c), is linear, while the color bar scale in the bottom row, panels (d–f) is logarithmic. The white arrows point to the cool plasma, cyan arrows point to the jet spire, and green arrows point to the jet-base region.

geometry will help us to understand the jet formation and eruption mechanism.

Here we show the magnetic field topology of jet-4 of Table 1 (Figure 9). In the upper panel of Figure 9, the red and blue extrapolated loops, respectively, represent the positive and negative photospheric magnetic fields. The green arrows point to the far-reaching magnetic field along which the jet material escapes outward and appears as a bright jet spire, in the same direction as the far-reaching magnetic field, in the synthetic Fe IX/Fe X images of Figure 5(b). The bottom panel shows the magnetic field geometry during the jet onset, at $t = 3500$ s, at a relatively different angle than the above image. This facilitates us to see the different sets of magnetic field lines at different angles. The orange arrow points to the closed field lines that are anchored above the neutral line. These closed field lines are the lower product of magnetic reconnection and a site of jet base brightening Fe IX/Fe X images of Figure 5(c). The JBP often appears at the location of an erupting minifilament (green arrows in Figures 2(e) and 5(c)). It is a miniature version of a solar flare arcade where downflows are often dominant (Imada et al. 2013).

4. Discussion

We selected five quiet Sun region small-scale coronal jets using HRI_{EUV} images, and investigated their origin using SDO/AIA and SDO/HMI data. In addition, we compared the observed jets with five analogous small-scale jets that we found in a Bifrost MHD simulation of a quiet Sun region. Overall, all five jets from the simulation show similarities with the jets from HRI_{EUV} and SDO/AIA observations. All of these jets show a resemblance with our earlier findings of typical coronal jets. The main difference is the size scale. The average base width of EUJ jets is 2200 ± 850 km, which is much smaller than the average base widths of typical coronal jets (12000 km; Panesar et al. 2018a). The base widths of our EUJ jets are similar to the sizes of the jets reported by Hou et al. (2021). Some of our jets may be considered as “jet-like” campfires reported by Panesar et al. (2021), but these are different from dot-like and loop-like campfires (Berghmans et al. 2021; Tiwari et al. 2022) because these jets are much bigger elongated structures moving outwards with enhanced base brightenings.

The sizes of our EUJ jets are not very different from the sizes of our jets in the Bifrost simulation. On average, the spire length

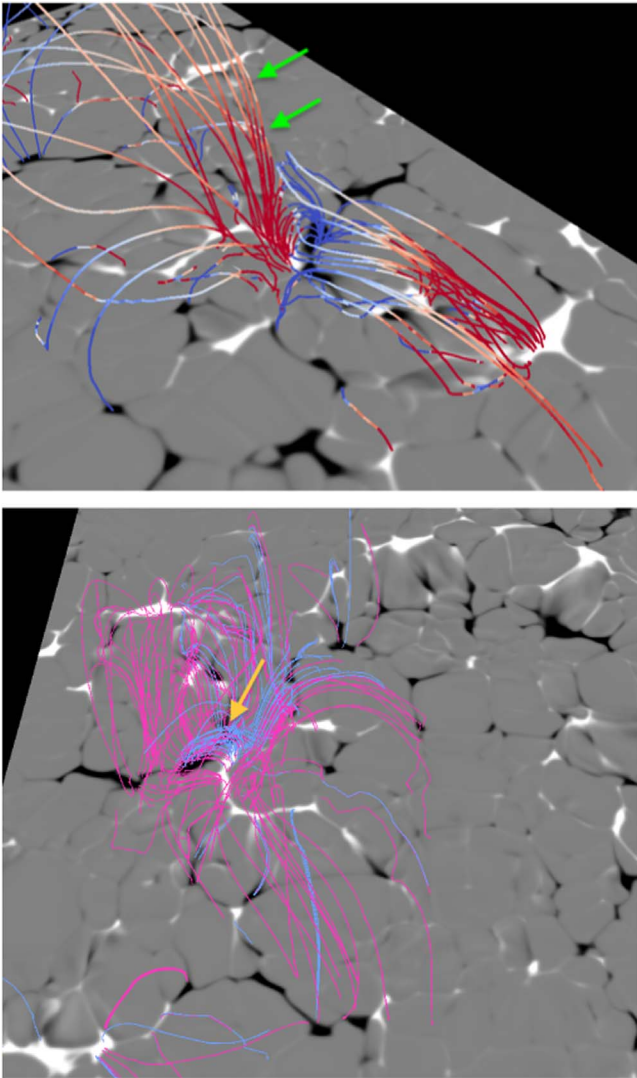


Figure 9. Magnetic field topology of the jet shown in Figure 5. The upper panel shows the 3D magnetic field geometry for the jet. The background image is a B_z map that is saturated at ± 500 G. The red and blue lines in the upper panel represent the positive and negative magnetic fields, respectively. The green arrows point to the newly-reconnected far-reaching magnetic field lines along which the jet material escapes. The bottom panel shows magnetic field topology from a different angle during the jet onset ($t = 3500$ s). The orange arrow points to the low-lying closed loops, near the location of the JBP. We used a different color combination in the bottom panel for drawing field lines for a better visual of the loops pointed to by the orange arrow.

of the EUJ jets is 6050 ± 2900 km whereas the jets in the simulation have a spire length of 6500 ± 2900 km, which are quite similar. The observed spire lengths are smaller than the lengths of IRIS jetlets (16000 km; Panesar et al. 2018b), Hi-C jets (9000 km; Panesar et al. 2019), and EUJ microjets (7700 km; Hou et al. 2021). The base width of our EUJ jets (2200 ± 850 km) is a little bit smaller than the base width of simulated jets (3900 ± 2100 km) and IRIS jetlets (4400 km; Panesar et al. 2018b). But it is larger than the base widths of campfires (1600 km; Panesar et al. 2021). The average speed of our jets in observations (60 ± 8 km s $^{-1}$) is in the same order as that for the jets in simulation (42 ± 20 km s $^{-1}$). On average, the simulated jets are a little bit slower than in observations. This could be due to the limited height of the simulated box. The average lifetime of our small-scale jets is 6.5 minutes, which is somewhat similar to the duration of simulated jets (9.0 minutes)

and two times longer than that of IRIS jetlets (3 minutes; Panesar et al. 2018b). The temporal cadence of the simulation is 50 s as compared to that of 10 s in the EUJ observations, resulting in the selection of the jets with relatively longer lifetimes in our simulation. That means, statistically, the observed and simulated jets perhaps have very similar lifetimes.

The reported jets here show qualitative similarities with typical coronal jets, and thus are “small-scale” coronal jets. All our jet physical parameters (e.g., spire lengths, base widths, and lifetimes) are significantly smaller than those for typical coronal jets, on average. As discussed above the observed parameters of jets in the simulation are almost similar to the parameters of EUJ jets. This gives us an opportunity to better understand the dynamics of small-scale coronal jets in high-resolution simulations.

Essentially all of our EUJ jets originate from magnetic neutral lines. Three out of five jets occur at the site of flux cancellation, consistent with the findings of Panesar et al. (2016b) for typical quiet Sun jets. In two events, we noticed that opposite flux is present at the jet-base region but its convergence toward the neutral line and then cancellation is not clear enough. This might be due to the fact that we are looking at the detection limit of HMI magnetograms.

The Bifrost simulation plays an important role in our study as it clearly shows the photospheric evolution of these small-scale jets, and the plasma flows in them. Four out of five jets occur at neutral lines where both the opposite polarity flux patches were present and the jets occurred during the process when positive and negative flux patches converged toward the neutral line, reconnect, and cancel with each other. We surmise that this is a reconnection-driven flux cancellation where flux cancellation is a consequence of the submergence of the lower product of the reconnected loops into the photosphere (van Ballegoijen & Martens 1989; Priest & Syntelis 2021; Syntelis & Priest 2021; Hassanin et al. 2022); a clear example of this mechanism can be found in Tiwari et al. (2014). This is apparently in agreement with our present and earlier jet observations that magnetic reconnection-driven flux cancellation, between majority-polarity flux and a merging minority-polarity flux patch, is the main cause of the formation and triggering mechanism of many coronal jets (Panesar et al. 2016b, 2018b). To the best of our knowledge, this is the first time that coronal jets are reported to systematically accompany magnetic flux cancellation in any 3D MHD simulation.

However, one jet in our simulation comes from a location where no magnetic field was present. Probably, there is some other mechanism that leads to this jet. In the simulation, we also notice that flux convergence and cancellation often occur at the edges of network regions and jets appear at some of these locations. We interpret that to have a coronal jet first we need to have a shear field and flux rope present at the neutral line. Panesar et al. (2017) found that pre-jet minifilaments mainly appear above sheared canceling neutral lines. Thus, no jets with minifilaments can occur at a neutral line in a potential bipolar magnetic field configuration. The above-mentioned scenario is similar to the formation and eruption mechanism of typical solar filaments (van Ballegoijen & Martens 1989; Moore & Roumeliotis 1992). Nonetheless, flux cancellation plays a significant role in the formation of small-scale jets as evident from our analyzed jets from the observations and simulation.

The magnetic field geometry of our jets in the Bifrost MHD simulation shows the formation of a small-scale loop at the

neutral line during the jet. We infer that this small-scale loop is the lower product of magnetic reconnection as it appears above the neutral line during the jet onset. The jet base brightening often appears at the neutral line during the jet onset (Sterling et al. 2015).

Apart from one event, the remaining four jets in the Bifrost simulation show evidence of chromospheric cool gas/plasma. The cool plasma is seen when the jet is lifting off and the jet spire shows the signature of both cool and hot plasma during the eruption, as previously noted in observations by Moore et al. (2013). The erupting cool plasma is evidence of a twisted flux rope that might be present at canceling neutral line. This is in agreement with our HRI_{EUV} and AIA jet observations where in three out of five cases a minifilament structure is seen. Some simulations have discussed the formation of the flux rope in typical coronal jets (e.g., Wyper et al. 2018; Doyle et al. 2019). We surmise that such small flux ropes might be produced in the simulation of this paper, leading to the jets via the above mechanism. However, further investigation is required to confirm this.

The opposite Doppler shifts (redshift and blueshift) have been seen in all five jets in the simulation, which is additional evidence of the untwisting motion in the magnetic field of the jet spire. The opposite Doppler shifts have been captured by the IRIS spectra in active region jets (e.g., Cheung et al. 2015; Lu et al. 2019; Ruan et al. 2019; Tiwari et al. 2019; Zhang et al. 2021). Recently, opposite Doppler shifts in an on-disk quiet region coronal jet have been observed by IRIS in Mg II k spectra (Panesar et al. 2022). The untwisting motions in the spire of coronal jets have also been reported in EUV observations (e.g., Moore et al. 2010; Schmieder et al. 2013; Panesar et al. 2016a).

We note that the structure of jets evolves and changes on the order of tens of seconds, which for their length scales means single slit rasters would be too slow to follow their evolution. Therefore, the characteristics of small-scale jets can be studied using an integral field spectrometer such as MUSE (Cheung et al. 2022; De Pontieu et al. 2022). The coordinated observations from DKIST, the Goode Solar Telescope, and SST together with MUSE would provide more information on the formation of small-scale coronal jets.

Our observations and simulation of small-scale jets show that jets frequently occur at the edges of quiet Sun network regions and their formation and eruption mechanisms are similar to those of typical coronal jets. HRI_{EUV} data gives us an opportunity to study and better understand the formation and eruption mechanism of small-scale jets. In the future, we will explore the formation mechanism of those jets that are not driven by minifilament eruption and are not visibly triggered by flux cancelation. Bifrost simulation of jets, with a larger spatial simulation domain and better cadence, will shed more light on the formation mechanism of coronal jets.

5. Conclusions

We analyze small-scale coronal jets using EUV 174 Å observations, and SDO data, and compare their properties with similar jets found in a Bifrost MHD simulation. Both the observations and simulation show a consistent picture of coronal jets in that majority of them form by magnetic reconnection accompanying flux cancelation at the neutral line. They also show evidence of cool plasma structure. These findings are in agreement with the observations of typical

coronal jets and larger-scale CME-producing eruptions. The observed small-scale jets most likely are miniature versions of them.

N.K.P. acknowledges support from NASA's SDO/AIA (NNG04EA00C) and HGI grant (80NSSC20K0720). S.K.T. gratefully acknowledges support from the NASA HGI grant (80NSSC21K0520) and NASA contract NNM07AA01C (Hinode). We acknowledge the use of Solar Orbiter/EUI and SDO/AIA/HMI data. AIA is an instrument on board the Solar Dynamics Observatory, a mission for NASA's Living With a Star program. Solar Orbiter is a space mission of international collaboration between ESA and NASA, operated by ESA. The EUI instrument was built by CSL, IAS, MPS, MSSL/UCL, PMOD/WRC, ROB, LCF/IO with funding from the Belgian Federal Science Policy Office (BELSPO/PRODEX); the Centre National d'Etudes Spatiales (CNES); the UK Space Agency (UKSA); the Bundesministerium für Wirtschaft und Energie (BMWi) through the Deutsches Zentrum für Luft- und Raumfahrt (DLR); and the Swiss Space Office (SSO). This work has made use of NASA ADSABS and Solar Software.

ORCID iDs

Navdeep K. Panesar  <https://orcid.org/0000-0001-7620-362X>
 Viggo H. Hansteen  <https://orcid.org/0000-0003-0975-6659>
 Sanjiv K. Tiwari  <https://orcid.org/0000-0001-7817-2978>
 Mark C. M. Cheung  <https://orcid.org/0000-0003-2110-9753>
 David Berghmans  <https://orcid.org/0000-0003-4052-9462>
 Daniel Müller  <https://orcid.org/0000-0001-9027-9954>

References

- Adams, M., Sterling, A. C., Moore, R. L., & Gary, G. A. 2014, *ApJ*, **783**, 11
 Alpert, S. E., Tiwari, S. K., Moore, R. L., Winebarger, A. R., & Savage, S. L. 2016, *ApJ*, **822**, 35
 Berghmans, D., Auchère, F., Long, D. M., et al. 2021, *A&A*, **656**, L4
 Carlsson, M., & Leenaarts, J. 2012, *A&A*, **539**, A39
 Chen, Y., Przybylski, D., Peter, H., et al. 2021, *A&A*, **656**, L7
 Cheung, M. C. M., Martinez-Sykora, J., Testa, P., et al. 2022, *ApJ*, **926**, 53
 Cheung, M. C. M., Pontieu, B. D., Tarbell, T. D., et al. 2015, *ApJ*, **801**, 83
 Chitta, L. P., Solanki, S. K., Peter, H., et al. 2021, *A&A*, **656**, L13
 Couvidat, S., Schou, J., Shine, R. A., et al. 2012, *SoPh*, **275**, 285
 Curdt, W., Tian, H., & Kamio, S. 2012, *SoPh*, **280**, 417
 De Pontieu, B., Hansteen, V. H., McIntosh, S. W., & Patsourakos, S. 2009, *ApJ*, **702**, 1016
 De Pontieu, B., Testa, P., Martinez-Sykora, J., et al. 2022, *ApJ*, **926**, 52
 Dere, K. P., Landi, E., Mason, H. E., Monsignori Fossi, B. C., & Young, P. R. 1997, *A&AS*, **125**, 149
 Doyle, L., Wyper, P. F., Scullion, E., et al. 2019, *ApJ*, **887**, 246
 Freeland, S. L., & Handy, B. N. 1998, *SoPh*, **182**, 497
 Gudiksen, B. V., Carlsson, M., Hansteen, V. H., et al. 2011, *A&A*, **531**, A154
 Hansteen, V., Guerreiro, N., Pontieu, B. D., & Carlsson, M. 2015, *ApJ*, **811**, 106
 Hansteen, V., Ortiz, A., Archontis, V., et al. 2019, *A&A*, **626**, A33
 Hansteen, V. H., Hara, H., De Pontieu, B., & Carlsson, M. 2010, *ApJ*, **718**, 1070
 Hassanin, A., Kliem, B., Seehafer, N., & Torok, T. 2022, *ApJL*, **929**, L23
 Hayek, W., Asplund, M., Carlsson, M., et al. 2010, *A&A*, **517**, A49
 Hou, Z., Tian, H., Berghmans, D., et al. 2021, *ApJL*, **918**, L20
 Imada, S., Aoki, K., Hara, H., et al. 2013, *ApJL*, **776**, L11
 Kabil, F., Hirzberger, J., Solanki, S. K., et al. 2022, *A&A*, **660**, A143
 Kamio, S., Curdt, W., Teriaca, L., Inhester, B., & Solanki, S. K. 2010, *A&A*, **510**, L1
 Kobayashi, K., Cirtain, J., Winebarger, A. R., et al. 2014, *SoPh*, **289**, 4393
 Lemen, J. R., Title, A. M., Akin, D. J., et al. 2012, *SoPh*, **275**, 17
 Li, D. 2022, *A&A*, **662**, A7
 Li, S., Jaroszynski, S., Pearse, S., Orf, L., & Clyne, J. 2019, *Atmos*, **10**, 488
 Lu, L., Feng, L., Li, Y., et al. 2019, *ApJ*, **887**, 154
 Mandal, S., Peter, H., Pradeep Chitta, L., et al. 2021, *A&A*, **656**, L16

- McGlasson, R. A., Panesar, N. K., Sterling, A. C., & Moore, R. L. 2019, *ApJ*, **882**, 16
- Moore, R. L., Cirtain, J. W., Sterling, A. C., & Falconer, D. A. 2010, *ApJ*, **720**, 757
- Moore, R. L., & Roumeliotis, G. 1992, in IAU Colloq. 133: Eruptive Solar Flares, ed. Z. Svestka, B. V. Jackson, & M. E. Machado (Berlin: Springer), 69
- Moore, R. L., Sterling, A. C., Falconer, D. A., & Robe, D. 2013, *ApJ*, **769**, 134
- Müller, D., Nicula, B., Felix, S., et al. 2017, *A&A*, **606**, A10
- Müller, D., St. Cyr, O. C., Zouganelis, I., et al. 2020, *A&A*, **642**, A1
- Panesar, N. K., Sterling, A. C., & Moore, R. L. 2016a, *ApJL*, **822**, L23
- Panesar, N. K., Sterling, A. C., & Moore, R. L. 2017, *ApJ*, **844**, 131
- Panesar, N. K., Sterling, A. C., & Moore, R. L. 2018a, *ApJ*, **853**, 189
- Panesar, N. K., Sterling, A. C., Moore, R. L., et al. 2018b, *ApJL*, **868**, L27
- Panesar, N. K., Sterling, A. C., Moore, R. L., et al. 2019, *ApJL*, **887**, L8
- Panesar, N. K., Sterling, A. C., Moore, R. L., & Chakrapani, P. 2016b, *ApJL*, **832**, L7
- Panesar, N. K., Tiwari, S. K., Berghmans, D., et al. 2021, *ApJL*, **921**, L20
- Panesar, N. K., Tiwari, S. K., Moore, R. L., & Sterling, A. C. 2020, *ApJL*, **897**, L2
- Panesar, N. K., Tiwari, S. K., Moore, R. L., Sterling, A. C., & De Pontieu, B. 2022, *ApJ*, **939**, 25
- Pike, C. D., & Mason, H. E. 1998, *SoPh*, **182**, 333
- Priest, E. R., & Syntelis, P. 2021, *A&A*, **647**, A31
- Rachmeler, L. A., Winebarger, A. R., Savage, S. L., et al. 2019, *SoPh*, **294**, 174
- Raouafi, N.-E., & Stenborg, G. 2014, *ApJ*, **787**, 118
- Rochus, P., Auchere, F., Berghmans, D., et al. 2020, *A&A*, **642**, A8
- Ruan, G., Schmieder, B., Masson, S., et al. 2019, *ApJ*, **883**, 52
- Scherrer, P. H., Schou, J., Bush, R. I., et al. 2012, *SoPh*, **275**, 207
- Schmieder, B., Guo, Y., Moreno-Insertis, F., et al. 2013, *A&A*, **559**, A1
- Schou, J., Scherrer, P. H., Bush, R. I., et al. 2012, *SoPh*, **275**, 229
- Shen, Y., Liu, Y., Su, J., & Deng, Y. 2012, *ApJ*, **745**, 164
- Skartlien, R. 2000, *ApJ*, **536**, 465
- Sterling, A. C., Harra, L. K., Moore, R. L., & Falconer, D. A. 2019, *ApJ*, **871**, 220
- Sterling, A. C., Moore, R. L., Falconer, D. A., & Adams, M. 2015, *Natur*, **523**, 437
- Sterling, A. C., Moore, R. L., Falconer, D. A., Panesar, N. K., & Martinez, F. 2017, *ApJ*, **844**, 28
- Syntelis, P., & Priest, E. R. 2021, *A&A*, **649**, A101
- Tiwari, S. K., Alexander, C. E., Winebarger, A. R., & Moore, R. L. 2014, *ApJL*, **795**, L24
- Tiwari, S. K., Hansteen, V. H., De Pontieu, B., Panesar, N. K., & Berghmans, D. 2022, *ApJ*, **929**, 103
- Tiwari, S. K., Moore, R. L., De Pontieu, B., et al. 2018, *ApJ*, **869**, 147
- Tiwari, S. K., Panesar, N. K., Moore, R. L., et al. 2019, *ApJ*, **887**, 56
- van Ballegoijen, A. A., & Martens, P. C. H. 1989, *ApJ*, **343**, 971
- Winebarger, A. R., Walsh, R. W., Moore, R., et al. 2013, *ApJ*, **771**, 21
- Wyper, P. F., DeVore, C. R., & Antiochos, S. K. 2018, *ApJ*, **852**, 98
- Young, P. R., Del Zanna, G., Landi, E., et al. 2003, *ApJS*, **144**, 135
- Zhang, Q. M., Huang, Z. H., Hou, Y. J., et al. 2021, *A&A*, **647**, A113
- Zhukov, A. N., Mierla, M., Auchère, F., et al. 2021, *A&A*, **656**, A35